Progress In Electromagnetics Research, Vol. 142, 243–260, 2013

ELECTROMAGNETIC ISOLATION OF A MICROSTRIP BY EMBEDDING IN A SPATIALLY VARIANT ANISOTROPIC METAMATERIAL

Raymond C. Rumpf[1, *], Cesar R. Garcia[1], Harvey H. Tsang[2], Julio E. Padilla[3], and Michael D. Irwin[2]

[1]EM Lab, W. M. Keck Center for 3D Innovation, University of Texas at El Paso, El Paso, Texas, USA

[2]W. M. Keck Center for 3D Innovation, University of Texas at El Paso, El Paso, Texas, USA

[3]Dr. Noveron Research Group, University of Texas at El Paso, El Paso, Texas, USA

Abstract—The near-field surrounding devices can be arbitrarily sculpted if they are embedded in a spatially variant anisotropic metamaterial (SVAM). Our SVAMs are low loss because they do not contain metals and are extraordinarily broadband, working from DC up to a cutoff. In the present work, a microstrip transmission line was isolated from a metal object placed in close proximity by embedding it in a SVAM so that the field avoided the object. Our paper begins by outlining a simple model for studying transmission lines embedded in SVAMs. We then present our design and experimental results to confirm the concept.

1. INTRODUCTION

3D printing is poised to revolutionize manufacturing [1] and transform the way electronics and electromagnetic devices are designed and manufactured. It offers the ability to arbitrarily place different materials in three dimensions with high precision. This will enable us to break away from traditional planar designs and to utilize the third dimension like never before. More functions can be fit into the same amount of space, products with novel form factors can be more easily manufactured, interconnect can be routed more smoothly, interfaces

Received 3 July 2013, Accepted 21 August 2013, Scheduled 2 September 2013

* Corresponding author: Raymond C. Rumpf (rcrumpf@utep.edu).

can be better implemented, electrical and mechanical functions can be comingled, and entirely new device paradigms will be invented. When we depart from traditional planar topologies, however, many new problems arise like signal integrity, crosstalk, noise, and unintentional coupling between devices [2–5].

Many solutions have been proposed to reduce coupling and cross talk including via hole fences [6, 7], guarded ground tracks [8], step shaped transmission lines [9], and even faraday cages [10]. All of these approaches, however, use metals and can produce even more problems in the framework of a 3D system because the isolation structures themselves occupy space and limit how closely components can be placed. In the present work, we propose spatially variant anisotropic metamaterials (SVAMs) as an all-dielectric technique to mitigate these problems. Anisotropic materials possess a different dielectric response depending on the direction of the field. In such a case, the permittivity and/or permeability are described by tensors instead of scalar quantities. Inside an anisotropic medium, the fields tend to develop in the directions with the highest constitutive parameters. This can be confined to a single direction if the anisotropy is made uniaxial. By spatially varying the orientation of the anisotropy around a device, the near-field can be sculpted almost arbitrarily on a highly subwavelength scale. In fact, static fields can be sculpted the same way.

The degree to which fields can be sculpted inside SVAMs depends on the strength of the anisotropy, or birefringence, and how well the orientation can be spatially varied. Metamaterials are engineered composites composed of a periodic lattice of physical features that interact with the electromagnetic field to provide new and useful properties [11, 12]. They can provide very strong birefringence and, combined with 3D printing, provide a mechanism for spatially varying the orientation of the anisotropy [13]. Traditional metamaterials are composed of resonant metallic elements that produce very high loss [14, 15]. To overcome this, our SVAMs are all-dielectric so they can be composed of very low loss materials and even be monolithic. Further, our SVAMs are nonresonant so they are extraordinarily broadband, working from DC up to a cutoff where the structure becomes resonant.

In this paper, we present a simple and powerful numerical technique that makes it easy to study devices embedded in spatially variant anisotropic media. Many commercial solvers such as Ansys HFSS^{TM} can either not incorporate arbitrary anisotropy or it is prohibitively difficult to build spatially variant anisotropy into the model. We use our tool to study how the field surrounding a microstrip

transmission line can be sculpted by embedding it in a SVAM. We study the impact of the strength of the anisotropy as well as spatially varying the orientation of the anisotropy. Based on these findings, we demonstrate the concept experimentally by isolating a microstrip transmission line from a metal object placed in close proximity by embedding it in a specially designed SVAM.

2. MODELING APPROACH

2.1. Governing Equations

The fundamental mode in a transmission line is very close to TEM (transverse electromagnetic). In this case, the analysis reduces to an electrostatic problem and transmission lines can be modeled using the inhomogeneous Laplace's equation instead of the more rigorous wave equation. We start with Maxwell's divergence equation, the constitutive relation for the electric field in an anisotropic material, and the relation between the electric field and the scalar potential.

$$\begin{bmatrix} \frac{\partial}{\partial x} & \frac{\partial}{\partial y} \end{bmatrix} \begin{bmatrix} D_x(x,y) \\ D_y(x,y) \end{bmatrix} = 0 \tag{1}$$

$$\begin{bmatrix} D_x(x,y) \\ D_y(x,y) \end{bmatrix} = \varepsilon_0 \begin{bmatrix} \varepsilon_{xx}(x,y) & \varepsilon_{xy}(x,y) \\ \varepsilon_{yx}(x,y) & \varepsilon_{yy}(x,y) \end{bmatrix} \begin{bmatrix} E_x(x,y) \\ E_y(x,y) \end{bmatrix} \tag{2}$$

$$\begin{bmatrix} E_x(x,y) \\ E_y(x,y) \end{bmatrix} = -\begin{bmatrix} \partial/\partial x \\ \partial/\partial y \end{bmatrix} V(x,y) \tag{3}$$

We derive the inhomogeneous Laplace's equation by substituting Equation (2) into Equation (1) to eliminate the D field, and then substituting Equation (3) into this new expression to eliminate the E field.

$$\begin{bmatrix} \frac{\partial}{\partial x} & \frac{\partial}{\partial y} \end{bmatrix} \begin{bmatrix} \varepsilon_{xx}(x,y) & \varepsilon_{xy}(x,y) \\ \varepsilon_{yx}(x,y) & \varepsilon_{yy}(x,y) \end{bmatrix} \begin{bmatrix} \partial/\partial x \\ \partial/\partial y \end{bmatrix} V(x,y) = 0 \tag{4}$$

Given a solution to this equation, the E field can be computed using Equation (3) and then the D field computed using Equation (2). At this point, all of the fields surrounding the device are known, can be visualized, and can be used to calculate the transmission line parameters. First, we calculate the distributed capacitance C of the line by looking it at as a capacitor. Given the electric fields, the total energy U stored in this system is

$$U = \frac{1}{2} \iint\limits_A \left(\vec{D} \cdot \vec{E} \right) dxdy. \tag{5}$$

This integral is taken over the entire cross section of the transmission line and must encompass all of the field energy. The energy stored in a capacitor is related to its capacitance C and stored voltage V_0 through Equation (6).

$$U = CV_0^2/2 \tag{6}$$

Combining Equations (5) and (6) gives us an equation to calculate the distributed capacitance from the electric fields.

$$C = \frac{1}{V_0^2} \iint_A \left(\vec{D} \cdot \vec{E}\right) dxdy \tag{7}$$

Second, if the medium surrounding the transmission line has no magnetic response, we can calculate the distributed inductance L directly from the distributed capacitance C_{air} of the same transmission line embedded in air instead of the anisotropic dielectric. In this case, the velocity of the wave on the line is related to the transmission line parameters through $c_0 \cong 1/\sqrt{LC_{air}}$. Solving this for L yields

$$L = 1/\left(c_0^2 C_{air}\right). \tag{8}$$

Given the distributed inductance and capacitance, the characteristic impedance of the transmission line is

$$Z_0 = \sqrt{L/C} \tag{9}$$

and the propagation constant at frequency ω is

$$\beta = \omega\sqrt{LC}. \tag{10}$$

2.2. Numerical Solution to Equation (4)

The remaining challenge is obtaining the solution to Equation (4). We solved this using a simple finite-difference method. This approach approximates the derivatives using central finite-differences. To handle this in a straightforward manner, we staggered the position of E_x, E_y, and V across a two-dimensional (2D) grid. The position of these terms across a 4×4 grid is illustrated in Figure 1. The potential is located at the origin of each cell in the grid. The electric fields are positioned at the cell boundaries, but offset from the origin by a half cell.

After approximating the derivatives with finite-differences, each of Equations (1)–(3) are written once for every cell in the grid. Adopting the matrix operators presented in Refs. [16, 17], these large sets of equations can be written in block matrix form as

$$\begin{bmatrix}\mathbf{D}_x & \mathbf{D}_y\end{bmatrix} \begin{bmatrix}\mathbf{d}_x \\ \mathbf{d}_y\end{bmatrix} = 0, \tag{11}$$

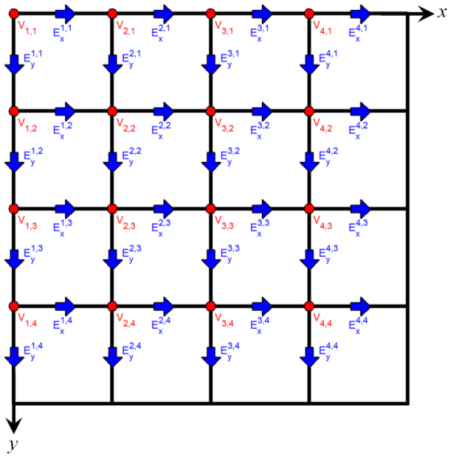

Figure 1. 4×4 grid for the finite-difference solution to Equation (4).

$$\begin{bmatrix} \mathbf{d}_x \\ \mathbf{d}_y \end{bmatrix} = \begin{bmatrix} \boldsymbol{\varepsilon}_{xx} & \mathbf{R}\boldsymbol{\varepsilon}_{xy} \\ \mathbf{R}^{\mathrm{T}}\boldsymbol{\varepsilon}_{yx} & \boldsymbol{\varepsilon}_{yy} \end{bmatrix} \begin{bmatrix} \mathbf{e}_x \\ \mathbf{e}_y \end{bmatrix}, \tag{12}$$

$$\begin{bmatrix} \mathbf{e}_x \\ \mathbf{e}_y \end{bmatrix} = - \begin{bmatrix} \mathbf{D}_x^{\mathrm{T}} \\ \mathbf{D}_y^{\mathrm{T}} \end{bmatrix} \mathbf{v}. \tag{13}$$

Here, $\mathbf{D}_x$ and $\mathbf{D}_y$ are banded matrices that calculate spatial derivatives of the electric fields across the staggered grid. The 'T' superscript indicates a transpose operation. The terms $\boldsymbol{\varepsilon}_{xx}$, $\boldsymbol{\varepsilon}_{xy}$, $\boldsymbol{\varepsilon}_{yx}$, and $\boldsymbol{\varepsilon}_{yy}$ are diagonal matrices containing the permittivity functions across the grid. The functions ε_{xx} and ε_{yx} are defined to be at the same points as E_x while the functions ε_{xy} and ε_{yy} are defined at the same points as E_y. $\mathbf{R}$ is a banded matrix that interpolates the E_y quantities to be at the same positions as the E_x quantities. $\mathbf{R}^{\mathrm{T}}$ is the transpose of $\mathbf{R}$ and interpolates E_x quantities to be at the same positions as the E_y quantities. The terms $\mathbf{d}_x$, $\mathbf{d}_y$, $\mathbf{e}_x$ and $\mathbf{e}_y$ are column vectors containing the field components D_x, D_y, E_x, and E_y respectively throughout the grid. Lastly, $\mathbf{v}$ is a column vector containing the scalar potential V throughout the grid. The matrix form of Equation (4) is derived by substituting Equation (12) into Equation (11) to eliminate $\mathbf{d}_x$ and $\mathbf{d}_y$, and then using Equation (13) to eliminate $\mathbf{e}_x$ and $\mathbf{e}_y$. The resulting block matrix equation can be written as

$$\mathbf{L}\mathbf{v} = 0, \tag{14}$$

$$\mathbf{L} = [\mathbf{D}_x \quad \mathbf{D}_y] \begin{bmatrix} \boldsymbol{\varepsilon}_{xx} & \mathbf{R}\boldsymbol{\varepsilon}_{xy} \\ \mathbf{R}^{\mathrm{T}}\boldsymbol{\varepsilon}_{yx} & \boldsymbol{\varepsilon}_{yy} \end{bmatrix} \begin{bmatrix} \mathbf{D}_x^{\mathrm{T}} \\ \mathbf{D}_y^{\mathrm{T}} \end{bmatrix}. \tag{15}$$

Equation (14) has only a trivial solution because we have not yet

defined the potential applied to the conductors. To do this, we construct a diagonal matrix $\mathbf{F}$ which has 1's in the diagonal positions corresponding to where conductors are placed on the grid. 0's are placed everywhere else. We further construct a column vector $\mathbf{v}_f$ which contains the voltages applied to each of the conductors identified in $\mathbf{F}$. Given these, we modify Equation (14) according to

$$\mathbf{L}'\mathbf{v} = \mathbf{b}, \tag{16}$$

$$\mathbf{L}' = \mathbf{F} + (\mathbf{I} - \mathbf{F})\,\mathbf{L}, \tag{17}$$

$$\mathbf{b} = \mathbf{F}\mathbf{v}_f. \tag{18}$$

We can now numerically solve Equation (16) as $\mathbf{v} = (\mathbf{L}')^{-1}\mathbf{b}$. Given $\mathbf{v}$, the E field components are calculated using Equation (13) and then the D field components calculated using Equation (12). After these functions are obtained, the distributed capacitance is calculated according to Equation (19).

$$C = \frac{\varepsilon_0 \cdot \Delta x \cdot \Delta y}{V_0^2} \begin{bmatrix} \mathbf{d}_x & \mathbf{d}_y \end{bmatrix} \begin{bmatrix} \mathbf{e}_x \\ \mathbf{e}_y \end{bmatrix}. \tag{19}$$

Note that the free space permittivity ε_0 was removed from Equation (12) and inserted here for convenience. The entire solution process is repeated with the dielectric set to air. In this case, Equation (15) reduces to the homogeneous Laplace's equation.

$$\mathbf{L}_h = \begin{bmatrix} \mathbf{D}_x & \mathbf{D}_y \end{bmatrix} \begin{bmatrix} \mathbf{D}_x^{\mathrm{T}} \\ \mathbf{D}_y^{\mathrm{T}} \end{bmatrix} \tag{20}$$

From this, the distributed inductance L is calculated from the distributed capacitance C_{air} using Equation (8). Finally, the characteristic impedance and propagation constant are calculated using Equations (9) and (10), respectively.

2.3. Example and Benchmark

To demonstrate and benchmark the method described above, we analyzed an ordinary microstrip transmission line. The baseline design was obtained from the closed form expression in Ref. [18]. The width of the microstrip was $w = 4.0\,\mathrm{mm}$, thickness of the substrate was $h = 3.0\,\mathrm{mm}$, and the dielectric constant of the substrate was $\varepsilon_r = 9.0$. The impedance calculated analytically using these dimensions was $49\,\Omega$.

The grid strategy for the numerical analysis is illustrated in Figure 2. In practice, many more grid cells are needed. The grid cells representing the substrate are shown in gray while the cells in air

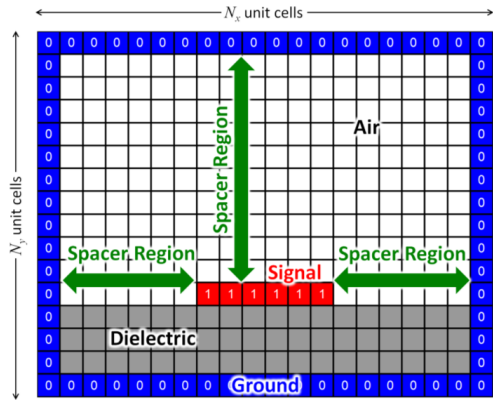

Figure 2. Grid strategy for finite-difference analysis of a microstrip transmission line.

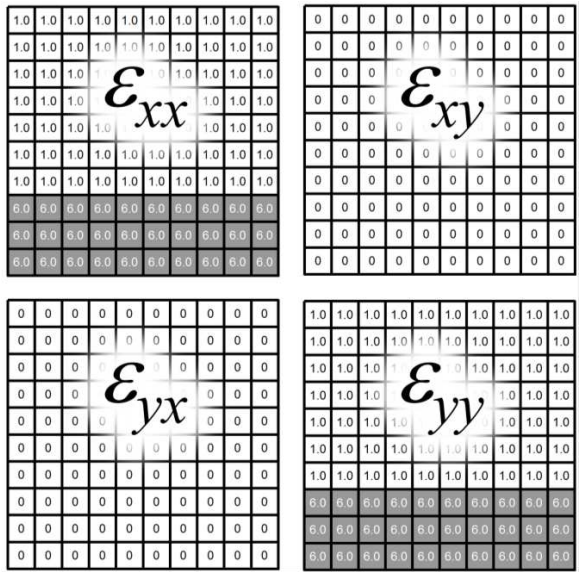

Figure 3. Four arrays describing the distribution of dielectric.

are shown in white. The grid cells corresponding to the signal trace are shown in red. The digit '1' in these cells indicates the potential is forced to $V_0 = 1.0\,\mathrm{V}$ at these points. The grid cells corresponding to the ground metals are shown in blue. The digit '0' in these cells indicates that the potential is forced to 0 V at these points. The entire outer boundary was set to ground as the boundary condition. As long as the spacer regions shown in green are made large enough, usually

3 to 5 line widths, the model converges to the properties of a real microstrip.

From this, we form four arrays describing the four dielectric tensor components (ε_{xx}, ε_{xy}, ε_{yx}, ε_{yy}). These arrays are depicted in Figure 3. This device has an isotropic substrate so the off-diagonal terms ε_{xy} and ε_{yx} are zero and the diagonal terms ε_{xx} and ε_{yy} are the same.

For this analysis, the actual number of grid cells used was $N_x = 211$ and $N_y = 180$ representing a region that was 70.3 mm × 60 mm. The size of the grid cells was $\Delta x = \Delta y = 0.3333$ mm. With these parameters, the line width was 12 cells and the substrate thickness was 9 cells. The results of this analysis are summarized in Figure 4. The finite-difference analysis predicted the characteristic impedance to be 46 Ω, which is very close to that predicted by the equation in Ref. [18]. The total calculation time was 11 seconds running on a single core of a 2.5 GHz Pentium i5 processor.

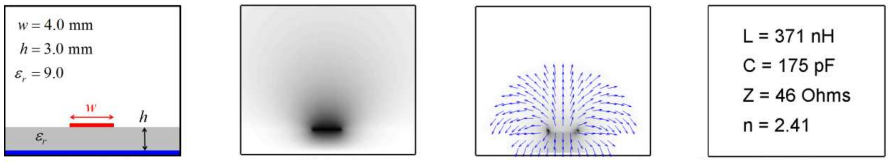

Figure 4. Numerical results for an ordinary microstrip. (a) Microstrip design. (b) Potential funtion $V(x, y)$. (c) Electric field $E(x, y)$. (d) Transmission line parameters.

3. MICROSTRIP EMBEDDED IN ANISOTROPIC MEDIA

We are now in a position to explore a microstrip embedded in anisotropic media. First, a series of simulations was performed to study the effect of the strength of the anisotropy, or birefringence, of the dielectric medium. We defined birefringence as $\Delta\varepsilon = \varepsilon_{xx} - \varepsilon_{yy}$ when the crystal axes are chosen so that the tensor is diagonal. The results of this analysis are provided in Figure 5. The distributed inductance was not affected because the electrostatic approximation decouples the magnetic field from the electric field. The distributed capacitance increased as the dielectric constant of the ε_{yy} tensor element was increased. This lowered the impedance of the transmission line as expected from Equation (9). The shape of the field was also affected by the increasing anisotropy. After observing the trend in Figure 5,

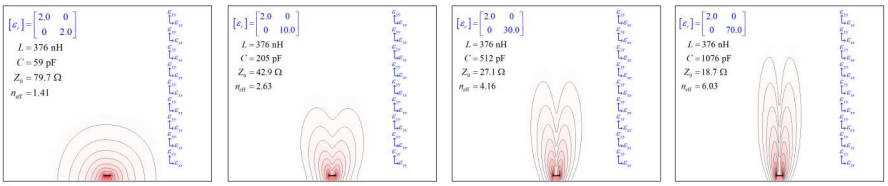

Figure 5. Study on the effect of the strength of the anisotropy of the surrounding medium. (a) Microstrip embedded in an isotropic medium. (b) Microstrip embedded in an anisotropic medium with $\Delta\varepsilon = 8.0$. (c) Microstrip embedded in an anisotropic medium with $\Delta\varepsilon = 28.0$. (d) Microstrip embedded in an anisotropic medium with $\Delta\varepsilon = 68.0$.

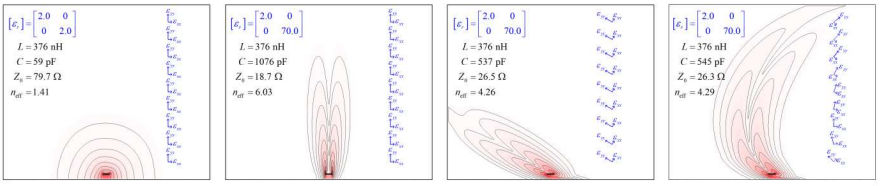

Figure 6. Study on the effect of the strength of spatially varying the anisotropy of the surrounding medium. (a) Microstrip embedded in an isotropic medium. (b) Microstrip embedded in an anisotropic medium. (c) Microstrip embedded in an anisotropic medium tilted by 60°. (d) Microstrip embedded in a spatially variant anisotropic medium.

we conclude that the field does tend to develop along the axis with the highest dielectric constant. Here, the field developed more strongly in the vertical direction because $\varepsilon_{yy} > \varepsilon_{xx}$. The degree to which this occurs was observed to be proportional to the birefringence.

Next, the effect of spatially varying the orientation of the anisotropy was studied in a series of simulations summarized in Figure 6. The first device is the same microstrip modeled previously, but with the dielectric constant set to 2.0. The second device was a transmission line embedded in an anisotropic medium with $\varepsilon_{xx} = 2.0$ and $\varepsilon_{yy} = 70.0$. The impedance of the line changed significantly after embedding in a SVAM so we conclude that transmission lines must be designed to be embedded. The shape of the field responded consistent with the discussion around Figure 5. For the third device shown in Figure 6(c), the orientation of the anisotropy around the transmission

line was tilted to the left by 60°. Consistent with the discussion above, the field shifted in this new direction. The impedance of the line increased somewhat due to the tilt. In the final device shown in Figure 6(d), the orientation of the anisotropy was spatially varied and the field still followed the anisotropy through the spatial variance. The impedance of this line changed only very slightly. This suggests that after a device is designed to be embedded in an anisotropic medium, the near-field can be arbitrarily sculpted using spatially variant anisotropy with minimal impact on the properties of the line.

To prove the concept in a more rigorous manner, a series of simulations was performed using Ansys HFSS^{TM}, which is a 3D full-wave electromagnetic field solver. A standard 50 Ω microstrip

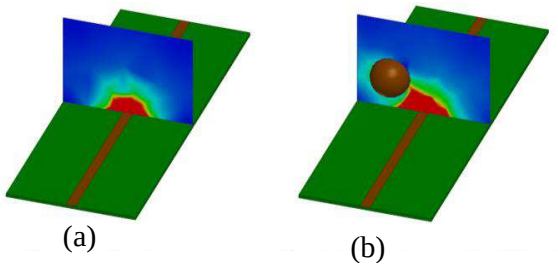

Figure 7. Rigorous 3D simulation of standard microstrip transmission line with and without a metal ball placed in close proximity. Transmission line parameters are the same as in Figure 4. (a) Microstrip line. (b) Microstrip line with metal object near.

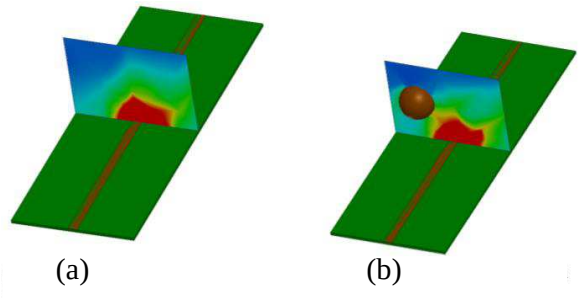

Figure 8. Rigorous 3D simulation of a microstrip embedded in an SVAM, with and without a metal ball placed in close proximity. Transmission line parameters are the same as in Figure 4. (a) Microstrip line embedded in an SVAM. (b) Embedded microstrip line with metal object near.

transmission line was designed on Rogers RT/Duroid®. The line was simulated with and without a metal ball placed in close proximity. Cross sections of the field from these simulations are shown in Figure 7. These show that the near-field of the transmission line shifts toward the metal ball when it is introduced.

Next, the microstrip was embedded in a SVAM where the anisotropy was rotated from the surface normal by 60° away from the metal ball. This was done to shift the field away from the ball so that its presence would not be felt by the microstrip. Cross sections of the field from these simulations are shown in Figure 8. In this case, the presence of the ball had much less effect on the shape of the near field, confirming our concept.

4. DEVICE DESIGN

4.1. Design of the Uniaxial Metamaterial

We began by designing an all-dielectric uniaxial metamaterial to provide the required anisotropy. It was a square array of high dielectric constant cylinders embedded in a low dielectric constant medium. This geometry was chosen because it is known to provide stronger anisotropy [13]. The SVAM was to be composed of polycarbonate (PC) thermoplastic backfilled with titanium dioxide (TiO_2) nano-powder. The dielectric constant of the PC was measured to be 2.33. The dielectric constant of the TiO_2 powder was estimated to be 40 using the Bruggeman model [19] and assuming the packing density was 64% by volume [20]. Based on these dielectric constants, the dielectric tensor can be quickly estimated using the Weiner bounds [21].

$$[\varepsilon_r] = \begin{bmatrix} \varepsilon_{xx} & 0 & 0 \\ 0 & \varepsilon_{yy} & 0 \\ 0 & 0 & \varepsilon_{zz} \end{bmatrix} \tag{21}$$

$$\frac{1}{\varepsilon_{xx}} = \frac{1}{\varepsilon_{zz}} = \frac{f_o}{\varepsilon_{r1}} + \frac{1 - f_o}{\varepsilon_{r2}} \tag{22}$$

$$\varepsilon_{yy} = f_e \varepsilon_{r1} + (1 - f_e)\, \varepsilon_{r2} \tag{23}$$

With optimized dimensions, the weight terms in the above equations are $f_o \cong 0.72$ and $f_e \cong 0.72$ and we get $\varepsilon_{xx} = 7.24$ and $\varepsilon_{yy} = 24.55$. In this work, rigorous values were obtained by modeling the unit cell with the plane wave expansion method (PWEM) [13, 22, 23]. Using the PWEM, the dimensions were optimized to maximize the birefringence. The lattice spacing a should be less than $\lambda/4$. In practice, this dimension should be made as small as possible so that the geometry of the unit cell still forms well after manufacturing. The optimum

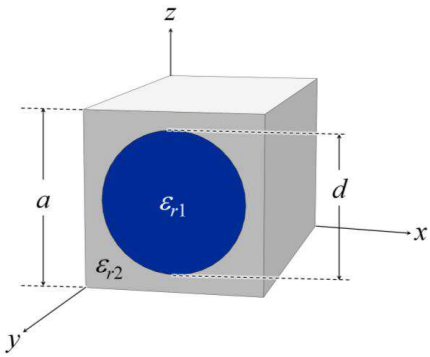

Figure 9. Cross section of the unit cell. For $\varepsilon_{r1} = 40$ and $\varepsilon_{r2} = 2.33$, the optimized dimensions are $d/a = 0.8$.

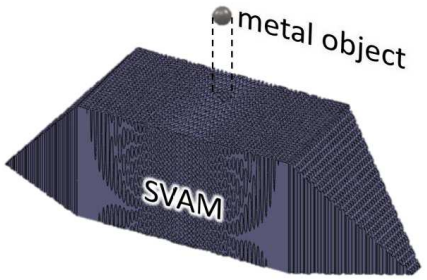

Figure 10. SVAM to be placed on top of an otherwise ordinary microstrip.

diameter of the cylinder was found to be $d = 0.84a$. This result is valid essentially independent of the choice of ε_{r1} and ε_{r2}. The resulting unit cell, shown in Figure 9, was predicted to have $\varepsilon_{xx} = 7.29$ and $\varepsilon_{yy} = 24.15$.

4.2. Design of the Spatial Variance

The SVAM was designed so that it could be placed on top of an otherwise ordinary mictrostrip. It was tapered at either end of the device to provide a smoother transition of impedance from the bare microstrip into the SVAM region. A small hole was formed through the device so that a metal ball could be inserted and located to within 2 mm of the microstrip. A CAD model of the SVAM is shown in Figure 10.

With the cylinders oriented vertically, the near-field around the line would develop vertically, like that shown in Figure 6(b). To move the field away from the ball, the cylinders were tilted away from the ball to an angle of 60° following a Gaussian profile. The device and the change in the orientation of the anisotropy is illustrated in Figure 11. For this simple design, it was not necessary to employ a more sophisticated design technique like transformation optics [24], but it is certainly possible to do this.

In order to spatially vary the orientation of the unit cells throughout a lattice without changing the size and shape of the unit cells, we used a novel algorithm to synthesize spatially variant lattices [25]. The algorithm is capable of spatially varying any

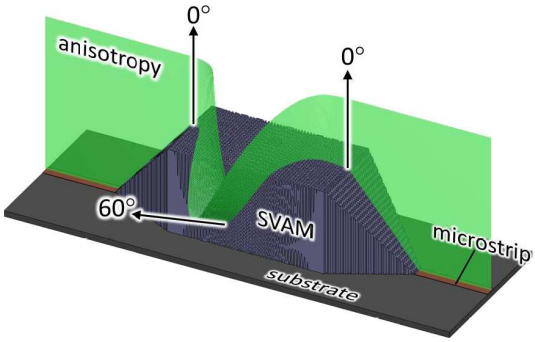

Figure 11. Orientation of the anisotropy of the SVAM.

combination of attributes of the lattice while still rendering the overall lattice smooth and continuous. Attributes include unit cell orientation, lattice spacing, fill fraction, material composition, geometry, and more. Avoiding discontinuities is important because these can cause scattering, field concentrations, and other detrimental effects.

5. EXPERIMENTAL RESULTS

5.1. Device Manufacturing

The SVAM was manufactured by 3D printing using a technique called fused deposition modeling (FDM) [1]. In this process, an inexpensive thermoplastic filament is fed through a print head where it is melted and deposited onto the surface of a platform. The print head is translated across the platform to deposit a layer of material in the desired pattern. After the layer is printed, the platform is lowered and the next layer is printed on top of the previous. This process is repeated for all layers until the part is complete. Several small test samples were printed to assess the minimum diameter of the holes so that they would form well in the final device. This was determined to be 2.0 mm. Photographs of the finished device are shown in Figure 12. In this device, the density of the holes is uniform. The density of the holes appears different throughout the device only because their orientation has been spatially varied and the device is shown from two different perspectives.

Next, the holes were packed with the TiO_2 nano-powder. First, a long wavelength vibrating table was used to shake the powder down into the holes. This achieved about a 95% fill. Second, the device was placed in an ultrasonicator to densify the powder.

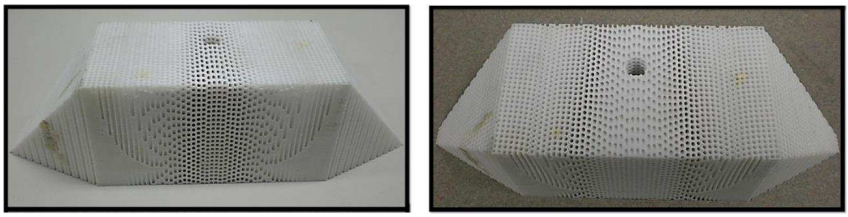

Figure 12. 3D printed spatially variant anisotropic metamaterial.

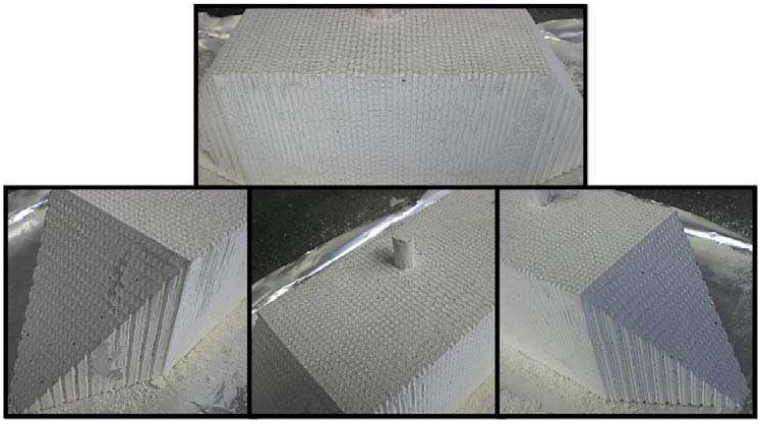

Figure 13. SVAM packed with TiO_2 nano-powder.

The remaining voids where filled by hand and then the device was placed back into the ultrasonicator one last time. Photographs of the packed SVAM are shown in Figure 13. The long term vision for this technology is to manufacture the entire circuit and SVAM completely by 3D printing. At present, no high dielectric constant material is commercially available for 3D printing so the TiO_2 powder was used instead.

5.2. Measured Results

To test the SVAM, a microstrip transmission line was designed specifically to be placed under the SVAM. The width of the line was made to be 10 mm so that it would be large relative to the periodic structure of the metamaterial. In practice, the SVAMs would be 3D printed with much finer dimensions so they can function around transmission lines having more typical dimensions. The microstrip was placed onto a cardboard substrate that was 2.8 mm thick. A ground

plane was placed under the cardboard. Pictures of the microstrip with and without the SVAM in place are shown in Figure 14.

The scattering parameters from the transmission line were measured using an Agilent N5245 PNA-X vector network analyzer. The data is shown in Figure 15. Little was done to match impedance so the return loss from the bare microstrip averaged around −15 dB. The dips in this spectrum arise from the Fabry-Perot resonance established between the connectors at either end of the line. When the SVAM was inserted, the spectrum shifted and reflection dropped by around 4 dB on the low frequency side. It is important to note that this data only shows the background reflection from the bare microstrip and SVAM. No metal ball was involved in these measurements.

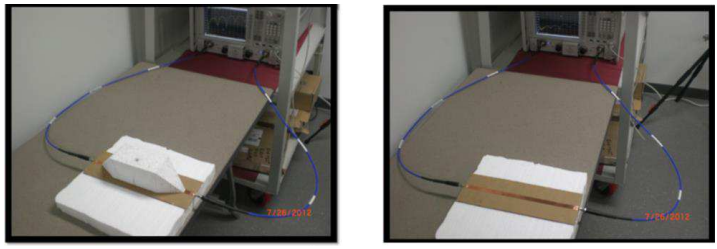

Figure 14. Microstrip transmission line in test setup, with and without the SVAM in place.

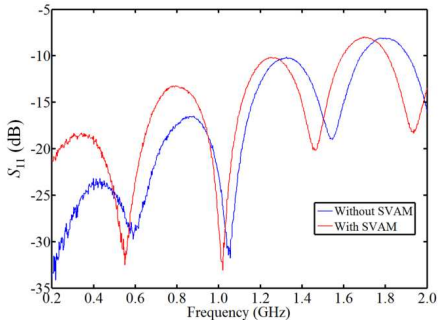

Figure 15. Reflection from the bare microstrip, with and without the SVAM in place.

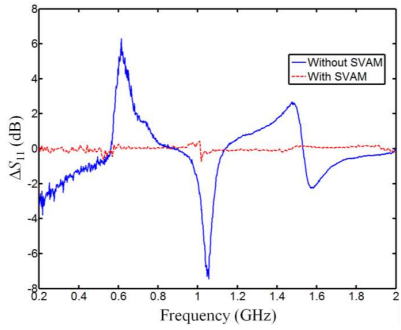

Figure 16. Change in S_{11} as ball is placed and removed for two cases: (1) solid blue line is for the microstrip in air, and (2) dashed red line is for the microstrip embedded in the SVAM.

From here, the scattering parameters of the bare microstrip were measured with and without the metal ball in place. The return loss of the microstrip and the insertion loss of the SVAM itself were calibrated out of the measurements so that only the effects of the metal ball were measured. The resulting change in S_{11}, with and without the ball in place, is plotted as a solid blue line in Figure 16. Fluctuations approaching 7 dB were measured. This same procedure was repeated, but with the SVAM in place. The change in S_{11} is plotted as a dashed red line in this same figure. For the second case, virtually no change in S_{11} was detected because the SVAM sculpted the field away from the ball. Fluctuations in this second curve were less than 0.5 dB.

6. CONCLUSIONS

3D printing will allow electronics and electromagnetics to break away from planar geometries and exploit the third dimension like never before. Placing and connecting components in three dimensions, however, presents many significant problems like signal integrity and crosstalk. In this paper, we propose for the first time using spatially variant anisotropic metamaterials as a means to sculpt the near-field around devices. To begin this study, we outlined a simple but powerful technique to study transmission lines embedded in spatially variant anisotropic media. This model was used to show that the near-field can be sculpted almost arbitrarily with minimal change to the properties of the device itself. This conclusion was confirmed with a rigorous 3D model. Based on these results, we isolated a microstrip transmission line from a metal ball placed in close proximity by embedding the line in a SVAM. The presence of the SVAM virtually eliminated any interference of the ball on the microstrip, confirming our new concept to manage fields in 3D printed systems.

While the present work focused on using SVAMs for isolation, the research suggests they can be used for other purposes such as enhanced coupling, improving the performance of components forced into awkward form factors, allowing antennas to radiate around and through other devices, and more.

ACKNOWLEDGMENT

This work was supported in part by a DARPA Young Faculty Award under Grant N66001-11-1-415. In addition, we would like to acknowledge the expertise contributed to this project by the W. M. Keck Center for 3D Innovation at the University of Texas at El Paso.

REFERENCES

1. Gibson, I., D. W. Rosen, and B. Stucker, *Additive Manufacturing Technologies: Rapid Prototyping to Direct Digital Manufacturing*, Springer, London; New York, 2010.
2. Gravelle, L. B. and P. F. Wilson, "EMI/EMC in printed circuit boards — A literature review," *IEEE Transactions on Electromagnetic Compatibility*, Vol. 34, No. 2, 109–116, 1992.
3. Hill, D. A., K. H. Cavcey, and R. T. Johnk, "Crosstalk between microstrip transmission lines," *IEEE Transactions on Electromagnetic Compatibility*, Vol. 36, No. 4, 314–321, 1994.
4. Isaacs, Jr., J. and N. Strakhov, "Crosstalk in uniformly coupled lossy transmission lines," *Bell Syst. Tech. J.*, Vol. 52, 101–115, 1973.
5. Xiao, F., W. Liu, and Y. Kami, "Analysis of crosstalk between finite-length microstrip lines: FDTD approach and circuit-concept modeling," *IEEE Transactions on Electromagnetic Compatibility*, Vol. 43, No. 4, 573–578, 2001.
6. Kim, J. H. and D. C. Park, "A simple method of crosstalk reduction by metal filled via hole fence in bent transmission lines on PCBs," *17th International Zurich Symposium on Electromagnetic Compatibility, EMC-Zurich 2006*, 363–366, 2006.
7. Ponchak, G. E., D. Chun, J.-G. Yook, and L. P. Katehi, "Experimental verification of the use of metal filled via hole fences for crosstalk control of microstrip lines in LTCC packages," *IEEE Transactions on Advanced Packaging*, Vol. 24, No. 1, 76–80, 2001.
8. Sharma, R. Y., T. Chakravarty, and A. B. Bhattacharyya, "Transient analysis of microstrip-like interconnections guarded by ground tracks," *Progress In Electromagnetics Research*, Vol. 82, 189–202, 2008.
9. Mallahzadeh, A. R., A. Ghasemi, S. Akhlaghi, B. Rahmati, and R. Bayderkhani, "Crosstalk reduction using step shaped transmission line," *Progress In Electromagnetics Research C*, Vol. 12, 139–148, 2010.
10. Wu, J. H., J. Scholvin, J. A. del Alamo, and K. A. Jenkins, "A Faraday cage isolation structure for substrate crosstalk suppression," *IEEE Microwave and Wireless Components Letters*, Vol. 11, 410–412, 2001.
11. Caloz, C. and T. Itoh, *Electromagnetic Metamaterials: Transmission Line Theory and Microwave Applications*, Wiley-IEEE Press, 2005.
12. Capolino, F., *Theory and Phenomena of Metamaterials,* 1st

edition, CRC Press LLC, 2009.

13. Garcia, C. R., J. Correa, D. Espalin, J. H. Barton, R. C. Rumpf, R. Wicker, and V. Gonzalez, "3D printing of anisotropic metamaterials," *Progress In Electromagnetics Research Letters*, Vol. 34, 75–82, 2012.
14. Khurgin, J. B. and G. Sun, "Scaling of losses with size and wavelength in nanoplasmonics and metamaterials," *Applied Physics Letters*, Vol. 99, 211106-1–211106-3, 2011.
15. Ponizovskaya, E., M. Nieto-Vesperinas, and N. Garcia, "Losses for microwave transmission in metamaterials for producing left-handed materials: The strip wires," *Applied physics Letters*, Vol. 81, No. 23, 4470–4472, 2002.
16. Rumpf, R. C., *Design and Optimization of Nano-optical Elements by Coupling Fabrication to Optical Behavior,* University of Central Florida, 2006.
17. Rumpf, R. C., "Simple implementation of arbitrarily shaped total-field/scattered-field regions in finite-difference frequency-domain," *Progress In Electromagnetics Research B*, Vol. 36, 221–248, 2012.
18. Poh, S., W. Chew, and J. Kong, "Approximate formulas for line capacitance and characteristic impedance of microstrip line," *IEEE Trans. Microwave Theory and Tech.*, Vol. 29, No. 2, 135–142, 1981.
19. Niklasson, G. A., C. Granqvist, and O. Hunderi, "Effective medium models for the optical properties of inhomogeneous materials," *Applied Optics*, Vol. 20, No. 1, 26–30, 1981.
20. Jaeger, H. M. and S. R. Nagel, "Physics of the granular state," *Science*, Vol. 255, No. 5051, 1523–1531, 1992.
21. Aspnes, D., "Local-field effects and effective-medium theory: A microscopic perspective," *American Journal of Physics*, Vol. 50, No. 8, 704, 1982.
22. Guo, S. and S. Albin, "Simple plane wave implementation for photonic crystal calculations," *Optics Express*, Vol. 11, No. 2, 167–175, 2003.
23. Johnson, S. G. and J. D. Joannopoulos, "Block-iterative frequency-domain methods for Maxwell's equations in a planewave basis," *Optics Express*, Vol. 8, No. 3, 173–190, 2001.
24. Pendry, J. B., D. Schurig, and D. R. Smith, "Controlling electromagnetic fields," *Science*, Vol. 312, No. 5781, 1780–1782, 2006.
25. Rumpf, R. C. and J. Pazos, "Synthesis of spatially variant lattices," *Optics Express*, Vol. 20, No. 14, 15263–15274, 2012.